

# Teleseismic Body-Wave Attenuation Beneath the Conterminous United States from Analysis of EarthScope Transportable Array data

Maximiliano J Bezada<sup>1</sup>, Joseph Stephen Byrnes<sup>1</sup>, Zhao Zhu<sup>1</sup>, and Hwaju Lee<sup>2</sup>

<sup>1</sup>University of Minnesota

<sup>2</sup>Seoul National University

December 7, 2022

## Abstract

Much information about the North American lithosphere has been gained by imaging seismic wave velocities. Additional constraints on the state of the subsurface can be gained by studying seismic attenuation, which has different sensitivity to physical properties. We produce a model of lateral variations in attenuation across the conterminous U.S. by analyzing P waveforms from deep earthquakes recorded by the EarthScope Transportable Array using a time-domain waveform matching approach. We divide the study area into 12 overlapping tiles and differential attenuation is measured in each tile independently; with analysis being repeated independently for 4 of the tiles. Measurements are combined into a smooth map using a linear inversion. Comparing results for adjacent tiles and for repeated tiles shows that the imaged features are robust. The final map is produced by combining all the measurements and shows generally higher attenuation west of the Rocky Mountain Front than east of it, with significant small length scale variations superimposed on that broad pattern. In general, there is a strong anticorrelation between differential attenuation and shear wave velocities at 90 km depth. However, a given change in velocity may correspond to large or small change in attenuation, depending on the area; suggesting that different physical mechanisms are operating. In some cases, most notably in the Snake River Plain, attenuation and velocity do not show the expected anticorrelation. The southern Intermountain Seismic Belt coincides with a high gradient in the attenuation signal, but even larger gradients further inland do not show any association with seismicity.

## Hosted file

USArrayAttenuationSuppInfo.docx available at <https://authorea.com/users/530520/articles/610924-teleseismic-body-wave-attenuation-beneath-the-conterminous-united-states-from-analysis-of-earthscope-transportable-array-data>

## Hosted file

essoar.10512766.1.docx available at <https://authorea.com/users/530520/articles/610924-teleseismic-body-wave-attenuation-beneath-the-conterminous-united-states-from-analysis-of-earthscope-transportable-array-data>

M. J. Bezada<sup>1</sup>, J. S. Byrnes<sup>2</sup>, Z. Zhu<sup>1</sup>, and H. Lee<sup>3</sup>

<sup>1</sup>University of Minnesota – Twin Cities.

<sup>2</sup>Northern Arizona University.

<sup>3</sup>Seoul National University.

Corresponding author: Maximiliano J. Bezada ([mbezada@umn.edu](mailto:mbezada@umn.edu))

Key Points:

- Teleseismic P attenuation is higher in the west than in the east of the conterminous U.S.
- Over this broad pattern, substantial short-wavelength heterogeneity exists.
- Attenuation is generally anticorrelated with velocity anomalies at 90 km depth, with some important exceptions.

Abstract

Much information about the North American lithosphere has been gained by imaging seismic wave velocities. Additional constraints on the state of the subsurface can be gained by studying seismic attenuation, which has different sensitivity to physical properties. We produce a model of lateral variations in attenuation across the conterminous U.S. by analyzing P waveforms from deep earthquakes recorded by the EarthScope Transportable Array using a time-domain waveform matching approach. We divide the study area into 12 overlapping tiles and differential attenuation is measured in each tile independently; with analysis being repeated independently for 4 of the tiles. Measurements are combined into a smooth map using a linear inversion. Comparing results for adjacent tiles and for repeated tiles shows that the imaged features are robust. The final map is produced by combining all the measurements and shows generally higher attenuation west of the Rocky Mountain Front than east of it, with significant small length scale variations superimposed on that broad pattern. In general, there is a strong anticorrelation between differential attenuation and shear wave velocities at 90 km depth. However, a given change in velocity may correspond to large or small change in attenuation, depending on the area; suggesting that different physical mechanisms are operating. In some cases, most notably in the Snake River Plain, attenuation and velocity do not show the expected anticorrelation. The southern Intermountain Seismic Belt coincides with a high gradient in the attenuation signal, but even larger gradients further inland do not show any association with seismicity.

Plain Language Summary

Seismic waves in the mantle propagate at lower speeds when temperatures are higher, rocks have higher water content, and small amounts of melt are present. These conditions also affect how much energy the wave loses as it passes through, which we call seismic attenuation. In this study we produce a map of seismic attenuation for the conterminous United States. We find that, in most places,

where seismic velocities are low, attenuation is high, and vice versa. This is what we would expect. Interestingly the size of the change in attenuation that corresponds to a given change in velocity varies by region. In a few places (most notably the Snake River Plain) variations in velocity don't correspond to variations in attenuation in the expected way. Some of the earthquakes that occur far from the plate boundary occur in regions where attenuation changes a lot over a small distance, but this is not always the case.

## 1 Introduction

Like all continents, North America is an amalgamation of lithospheric terranes of different ages, origins and characteristics that has been assembled around a cratonic core over billions of years (e.g. Whitmeyer & Karlstrom, 2007). The conterminous United States constitutes a large fraction of the North American continent and seismic data acquired by the EarthScope Transportable Array (TA) provided unprecedented data coverage of this region. The result has been the development of models of seismic properties with much higher resolution than previously possible, including the detailed seismic characterization of the lithosphere-asthenosphere system at a continental scale. One of the more impactful legacies of the EarthScope initiative is the discovery of complexity and heterogeneity in the “stable” continental lithosphere east of the Rocky Mountains, far from any plate boundary regions.

Most products of the TA characterize the propagation velocity of seismic waves, whether through the constraint of absolute velocities, velocity anomalies, velocity contrasts, or velocity anisotropy (e.g. Buehler & Shearer, 2017; Hopper & Fischer, 2018; Lin & Schmandt, 2014; Porritt et al., 2021; Porter et al., 2016; Schmandt & Lin, 2014; Shen & Ritzwoller, 2016; Zhou et al., 2022). An additional and complementary observable is seismic attenuation. Attenuation has different and less well-understood sensitivity to the physical state of the subsurface (e.g., temperature, composition, and melt content) and thus can reduce the ambiguity that is inherent in the interpretation of seismic velocity structure. In contrast to the abundance of studies of seismic velocity of the North American lithosphere-asthenosphere system, studies of attenuation are scarce and often come with significant caveats. The model of Lawrence and Shearer (2006) predates the TA and has strong features that are hard to correlate to known geologic structure. The Cafferky and Schmandt (2015) model represents the state of the art for body wave attenuation, but the authors caution that it is difficult to establish the correct amount of smoothing for their data and that scattering, rather than attenuation, may be a strong driver of their results. A Rayleigh wave based study of attenuation by Bao et al. (2016) produces a model with much short wavelength variation that is difficult to interpret without substantial ad-hoc smoothing and the authors caution that their correction for the focusing and defocusing of the wavefield may not be accurate for the degree of heterogeneity in the conterminous United States.

In this study, we perform a time-domain analysis of direct P waveforms from deep earthquakes recorded by the TA stations to measure relative attenuation,

and combine those measurements into a two-dimensional model for the conterminous U.S. As expected, we find attenuation is generally higher west of the Rocky Mountain Front (RMF), but only to first order. Larger than expected changes in attenuation occur east of the RMF. Many of the attenuation anomalies correlate well with velocity anomalies but the proportionality constant between velocity and attenuation differs substantially in different regions, meaning a given change in velocity can correspond to either a small or large change in relative attenuation in different places, suggesting different sensitivity to the underlying physical parameters that are affecting the seismic observables.

## 2 Materials and Methods

We apply attenuation measurement and imaging techniques that have been successfully used recently in different settings (Bezada & Smale, 2019; Bezada, 2017; Byrnes et al., 2019; Byrnes & Bezada, 2020; Deng et al., 2021; Zhu et al., 2021). Compared to previous studies, the scale of the study area warrants the use of different strategies for data analysis and inversion for a smooth map, which we describe below.

### 2.1 General Approach

The goal of the study is to image lateral variation in attenuation over the conterminous United States, an area of  $\sim 8$  million  $\text{km}^2$  covered by the nearly 1800 stations of the TA in a  $\sim 70$  km spaced grid (Figure 1). To measure differential attenuation ( $\Delta t^*$ ) we use the time domain method of Bezada (2017), which is based on the work of Adams and Humphreys (2010). The least attenuated traces (as determined visually by the analyst) are stacked to produce an estimate of the source-time function and this estimate is numerically attenuated over a range of  $t^*$  to generate synthetic waveforms with different degrees of attenuation. The synthetics that best-fit the observed waveforms thus provide an estimate of  $\Delta t^*$ ; note that the absolute degree of attenuation in the initial estimated source-time function is not known and so only relative values can be constrained.

Two confounding factors are particularly relevant to this study. The first is directivity, which produces systematic variations in the width of the waveform with azimuth. This poses a challenge when applying the waveform matching approach over too large of an area because broadening of the waveforms by directivity may be misinterpreted as broadening of the waveforms by attenuation. Previous studies ignored directivity because the backazimuth is nearly constant for a small study area (Bezada, 2017; Byrnes et al., 2019; Byrnes & Bezada, 2020; Zhu et al., 2021); however this assumption is less valid when the method is applied at this spatial scale. A second confounding factor is the reliance on the analyst to identify which traces to include in the estimate of the unattenuated source-time function, and in quality control to accept or reject measurements based on the quality of the fit to the observed waveforms. These aspects could make the results subjective and raise questions on the dependence of the final model on choices made by individual analysts.

To address both of these challenges, we divide the study region into 12 overlapping tiles (Figure 1). Each tile encompasses 9.5 degrees of latitude by 16 degrees of longitude and has varying amounts of overlap with adjacent tiles (Figure 1). The locations of the tiles were chosen in an ad-hoc manner to conform to irregularities in the shape of the array which result from the location of national borders as well as the Atlantic and Gulf of Mexico coasts. The overlap between the tiles allows us to check for consistency between results at adjacent tiles processed by different analysts. Additionally, we choose 4 tiles for which the attenuation measurements are done by 2 different analysts; allowing for a direct comparison and assessment of how the final result depends on analyst choices. In total, 16 tiles are analyzed (12 individual tiles plus 4 repeats), with each of the 4 authors completing the analysis for 4 tiles.

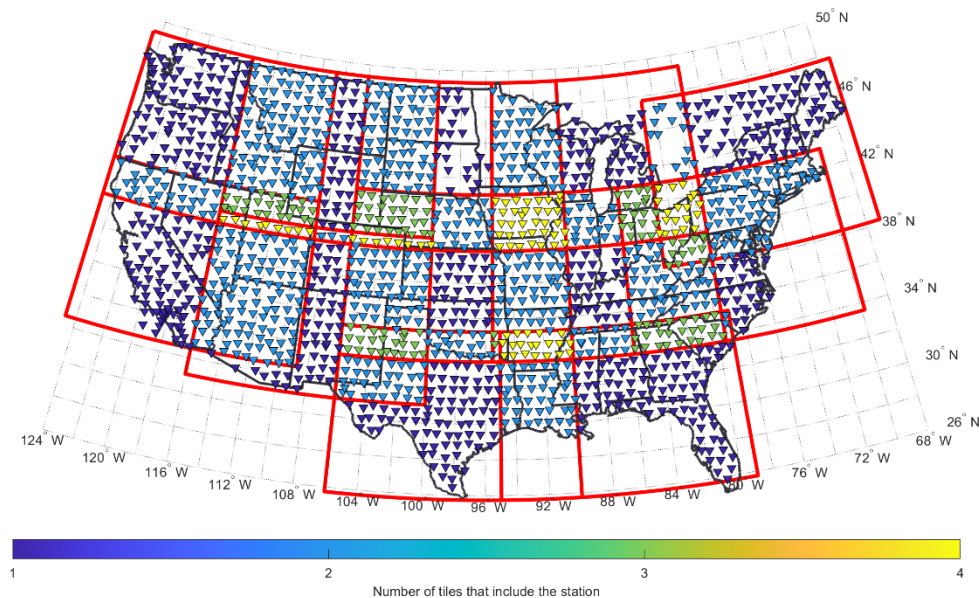


**Figure 1.** Spatial distribution of seismic stations used in this study (inverted triangles) and limits of the “tiles” into which the study area was divided (red lines). Seismic stations are color-coded according to the number of tiles in which they are included. Only stations that yielded  $\Delta t^*$  measurements are shown.

## 2.2 Stations and Events

In order to maintain even coverage across the study area we analyze data from the TA and the Southern California network but exclude FlexArray deployments. This results in a total of 1745 stations across the conterminous U.S. with a

station spacing of  $\sim 70$  km (Figure 1). The number of stations within each tile is variable, ranging from  $\sim 200$  to  $\sim 300$ . Most stations are included in more than 1 tile (Figure 1), with 44%, 8% and 5% being included in 2, 3 and 4 tiles, respectively. We utilize the vertical component velocity seismograms for measuring attenuation.

As in previous studies, we restrict events to those with hypocentral depths larger than 250 km. These events occur below the low-Q asthenosphere, and so are primarily attenuated on the receiver side. Moreover, deeper events typically have impulsive sources which makes them easier targets for waveform matching. Since we are using teleseismic direct P phases, we restrict the epicentral distances to 30-90 degrees from the center of each tile. Tiles in the west coast are in range of the more seismically prolific subduction zones and thus more earthquakes fitting our criteria are recorded there than in the tiles further east. In order to ensure suitable signal-to-noise ratios only events with magnitude  $> 5.5$  are examined. In total, the number of events matching the criteria for each tile range from 20 to over 100. Of these, the number of events that yielded useful  $\Delta t^*$  measurements in the different tiles ranges from 10 to  $> 50$ .

### 2.3 Measurement of $\Delta t^*$

As mentioned in section 2.1, we utilize the time domain  $\Delta t^*$  measurement method described in Bezada (2017). This method has been shown to be more robust than the traditional spectral ratio method of Teng (1968) (Bezada et al., 2019; Byrnes & Bezada, 2020). For each event, we produce an estimate of the unattenuated source waveform by selecting and stacking the traces with the most impulsive first arrivals. We find  $\Delta t^*$  for each recorded trace by comparing it with a numerically attenuated version of the estimated source waveform calculated with the attenuation operator of Azimi (1968) in the frequency domain:

$$A = \exp \left\{ -\omega \Delta t^* \left[ \frac{1}{2} + \frac{i}{\pi} \ln \left( \frac{\omega}{\omega_0} \right) \right] \right\}$$

where only the differential attenuation  $\Delta t^*$  affects the shape of the waveform. We grid-search over  $\Delta t^*$  values and choose the value that minimizes the L2 norm of the misfit between the numerically attenuated source trace and the observed waveform in a selected time window (Figure 2). The best-fitting synthetic waveform is visually inspected before accepting the  $\Delta t^*$  measurement.

Our procedure does not make any considerations for the frequency dependence of attenuation. Although a small frequency dependence is well documented in experiments (e.g. Jackson & Faul, 2010), the effect is small over the limited bandwidth of our data. Studies that have attempted to constrain frequency dependence of teleseismic body wave attenuation have shown that the results are nearly identical to those obtained assuming frequency independence (Cafferky & Schmandt, 2015; Eilon & Abers, 2017).

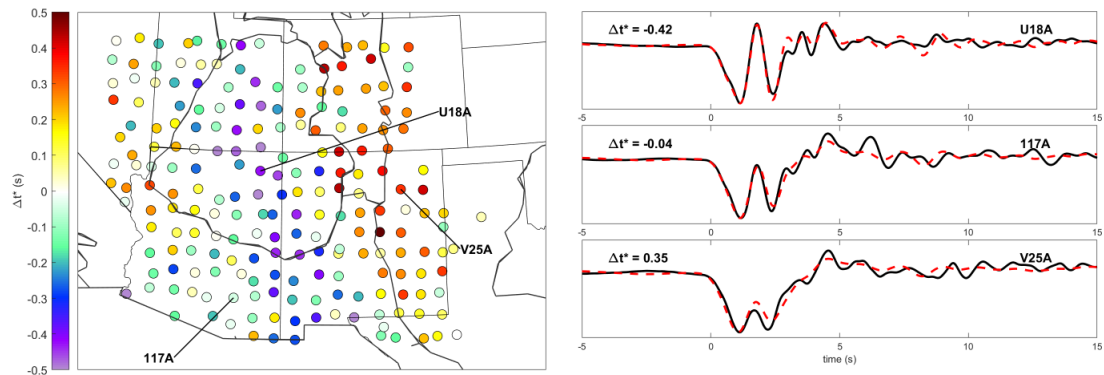


**Figure 2.**  $\Delta t^*$  measurements from one event recorded on tile B2 (encompassing the Colorado Plateau and its surroundings) along with example observed (black) and best-fit synthetic (dashed red) waveforms. Waveform panels include the measured value (in seconds) and the station name. Stations for which the waveforms are shown are indicated on the map.

#### 2.4 Construction of the Map

The measurements of  $\Delta t^*$  for any one event can show substantial scatter superimposed on the regional features (Figure 2), and the information from all the events needs to be combined to produce a robust map of lateral variations in attenuation. To this end, previous studies have used two different approaches: a linear inversion that solves for station statics (Bezada & Smale, 2019; Maximiliano J. Bezada, 2017) or a transdimensional Markov Chain Monte Carlo (TDMCMC) inversion (Byrnes et al., 2019; Deng et al., 2021; Zhu et al., 2021). The TDMCMC inversion is especially useful when station coverage is uneven because, having no set node spacing, the model parameterization (and thus its resolution) emerges from the data coverage. For this study, this advantage is not important because station coverage is even across the study area, and the linear inversion is thus suitable. The challenge with the linear inversion is selecting the optimal set of regularization parameters and characterizing the uncertainty. We use an inversion that includes advantages from both of the previously used methods in that each individual inversion is linear as described in Bezada (2017) but many inversions are performed and the optimal regularization parameters are found through a Bayesian scheme following the formalism of Malinverno and Briggs (2004). For more details on the method see the supplementary information.

### 3 Results

We present the results in three parts. First, we run the inversion procedure for each tile individually. We then show the results obtained by different analysts for specific tiles. Finally, we obtain the full model by running the inversion for the entire dataset consisting of the  $\Delta t^*$  measurements from all the tiles.

### 3.1 Individual Tiles

Results for each of the individual tiles show that the algorithm finds different regularization parameters for each tile which is reflected in the amplitude and roughness of the anomalies. Broadly speaking, the algorithm will prefer sharper and higher amplitude features when the  $t^*$  values are more internally consistent or when more data is available. However, patterns of low and high attenuation on the edges of the tiles where there is overlap are consistent between adjacent tiles (Figure 3). Tiles where the analysis was done independently by two different analysts also show consistent results (Figure 4), with the main difference being the amplitude and roughness of the anomalies, again reflecting differences in regularization. Spatial patterns of high and low attenuation seem thus to be robustly constrained by our analysis. We perform this exercise primarily to check for consistency, and consider the inversion of the ensemble dataset the preferred model.

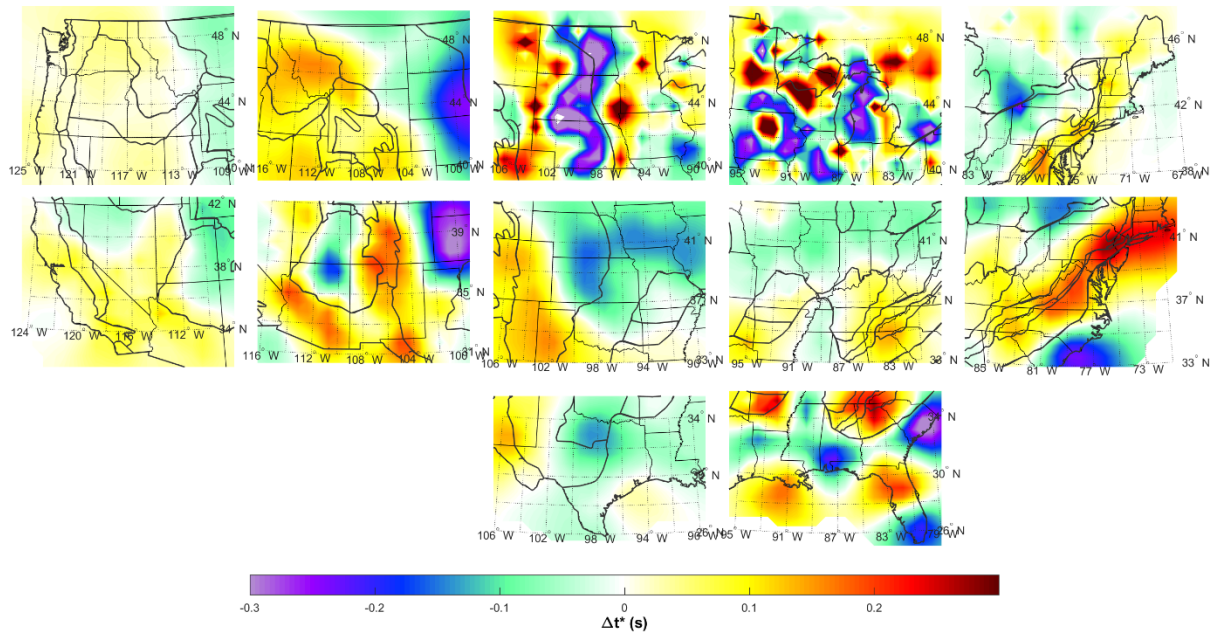


**Figure 3.**  $\Delta t^*$  maps resulting from the inversion of data from each individual tile separately. Thinner black lines show state boundaries, thicker black lines show tectonic province boundaries.

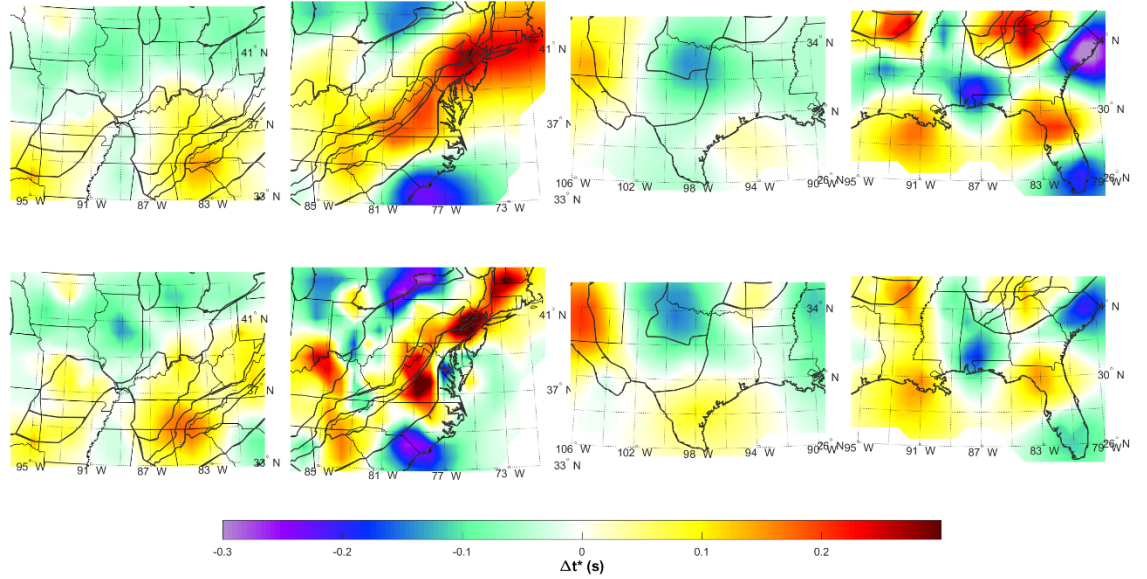


**Figure 4.** Comparison of  $\Delta t^*$  maps resulting from the inversion of data from each of the 4 tiles that were processed independently by two different analysts. The top and bottom rows correspond to results from inverting the measurements made by the first and second analyst, respectively. Note that for all tiles spatial patterns of low and high attenuation are consistent in the two independent analyses. Thinner black lines show state boundaries, thicker black lines show tectonic province boundaries.

### 3.2 Complete Model

The entire study region shows a range in  $\Delta t^*$  of roughly -0.25 to 0.25 s and, to first order, results broadly conform to the expectation of higher attenuation west of the RMF (Figure 5). However, low attenuation anomalies are found in the western U.S. and substantial high-attenuation anomalies are found in the eastern U.S.

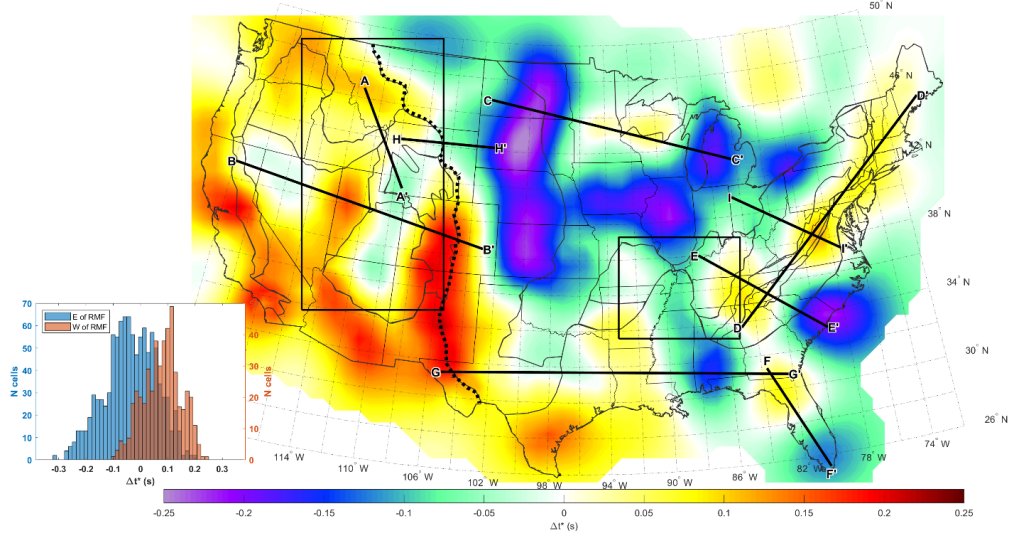


**Figure 5.**  $\Delta t^*$  maps resulting from the inversion of the entire set of measurements. Thinner black lines show state boundaries, thicker black lines show tectonic province boundaries. Also indicated in the figure are the locations of the profiles shown in Figure 7 and boxes in the west and the east of the study area show the locations of the smaller maps shown in Figure 9 and 10, respectively. Inset: Histogram of  $\Delta t^*$  values east and west of the Rocky Mountain Front (RMF) as defined by the thick dotted line on the map.

West of the RMF, we observe mostly high attenuation with a mean  $\Delta t^*$  value of 0.08 s and a standard deviation of 0.07 s (Figure 5, inset). Relatively low attenuation ( $\Delta t^*$  of -0.02 to -0.08 s) is observed in the core of the Colorado Plateau (CP) and further north in SW Wyoming (Figure 5). High attenuation values surround the CP on the remaining three sides (to the west, east and south) with the southern Rocky Mountains directly east of the CP showing some of the highest attenuation values in the whole model ( $\Delta t^*$  of up to 0.22 s). The central and NW great basin show average to slightly positive differential attenuation ( $\Delta t^*$  as low as 0.02 s). The NW U.S. (west of the RMF and north of  $\sim 43^\circ$  N) shows moderately high attenuation ( $\sim 0.1$  s) with some small fluctuations. Surprisingly, given the very low seismic velocities widely documented in this region (e.g. Schmandt & Lin, 2014; Shen & Ritzwoller, 2016; Stanciu & Humphreys, 2020), the eastern Snake River Plain and the Yellowstone area do not feature high attenuation, and the area is unremarkable in the attenuation map (Figure 5). In this model, we do not observe a clear low-attenuation region that one would expect to be associated with the Juan de Fuca slab. Directly south of  $\sim 39^\circ$  N where tomography models place the southern end of the slab (e.g. Bodmer et al., 2018; Hawley et al., 2016; Schmandt & Lin, 2014), our

model shows a very high attenuation anomaly ( $\Delta t^*$  of 0.18 to 0.24 s, Figure 5).

East of the RMF, attenuation is remarkably heterogeneous. We find alternating high and low attenuation anomalies with length scales on the order of  $\sim 200$  to  $\sim 1,000$  km. A notable 200-300 km wide low-attenuation anomaly ( $\Delta t^*$  of -0.14 to -0.26 s) extends roughly N-S from the northern end of the model at  $50^\circ$  N to near the Oklahoma-Kansas border at  $\sim 36.5^\circ$  N (Figure 5). East of this anomaly, relatively high attenuation is observed at  $44^\circ$  to  $47^\circ$  N with peaks that reach  $\Delta t^*$  values of 0.08 s over the states of Minnesota and Wisconsin and a local minimum between these attenuation peaks that coincides with the axis of the mid-continent rift. Attenuation is again low east of Lake Michigan (as low as -0.18 s). Attenuation is also low directly south of the Minnesota-Wisconsin anomalies and further south the model shows mildly negative to neutral attenuation; with the exception of mildly positive attenuation anomalies beneath the Texas and Louisiana Gulf Coast and another anomaly roughly centered on  $35^\circ$  N and  $93^\circ$  W.

In the eastern U.S., the Appalachians are characterized by a band of moderately high attenuation (comparable to values in the NW U.S.) punctuated by three local maxima in the southern, central, and northern Appalachians where  $\Delta t^*$  values are as high as 0.14 s. A very low attenuation block (with some of the lowest values in the entire model,  $\Delta t^*$  of -0.18 to -0.3 s) is seen east of the Appalachian piedmont in South Carolina. Significantly low attenuation is also observed in southern Florida, south of  $\sim 27.5^\circ$  N and in the central Gulf Coast between  $86^\circ$  and  $88^\circ$  W, in both cases reaching a minimum value of -0.18 s.

#### 4 Discussion

In this section we explore how the imaged attenuation structure relates to other observations, with a focus on what we consider to be the most noteworthy anomalies.

##### 4.1 Relationship to Velocity Structure

Theory dictates that seismic velocity and quality factor should correlate, and hence  $t^*$  should anti-correlate with velocity anomalies. Laboratory experiments have constrained the relationship between velocity and quality factor for changes in temperature and grain size under upper mantle conditions (e.g. Faul & Jackson, 2005; Jackson & Faul, 2010). The effect of melt and volatiles is less well known and still debated, but studies typically predict these factors lead to an anticorrelation between velocity and  $t^*$  (Chantel et al., 2016; Faul et al., 2004; Yamauchi & Takei, 2016) with some exceptions (Cline II et al., 2018; Hammond & Humphreys, 2000). Seismic velocity models of the conterminous U.S. are abundant, and the similarity between different models suggests the results are robust (e.g. Becker, 2012; Pavlis et al., 2012). We choose to anchor our discussion of the features in our attenuation model on how they relate (or don't) to features in the velocity models, using the body wave model of Schmandt and Lin (2014) and the surface-wave model of Shen and Ritzwoller (2016).

While velocity models constrain the variations in seismic properties in three dimensions, the differential attenuation measurements we present are path-integrated and thus have no intrinsic control on variations in  $Q$  with depth. Previous studies, however, have shown that the anticorrelation between velocity structure and attenuation is strongest at depths of 100-200 km (Byrnes et al., 2019; Liu et al., 2022; Zhu et al., 2021) and that attenuation is well correlated with lithospheric thickness (Deng et al., 2021). This suggests that lateral variations in attenuation dominantly reflect lateral variations in the lithosphere-asthenosphere system which are well-captured by the velocity structure at  $\sim 100$  km depth.

For the attenuation model we present here, we also find a strong anti-correlation with seismic velocity at depths typical of the lithosphere and asthenosphere (Figure 6). We calculate the correlation coefficient by resampling two different P and S velocity models at each depth at the locations of grid points in our model. We thus get the correlation coefficient as a function of depth and find a peak value of  $-0.6$  for both P and S velocities with the model of Shen and Ritzwoller (2016) at 120 km depth and of  $-0.5$  for P and  $-0.56$  for S velocities at a depth of 60 km in the model of Schmandt and Lin (2014). In the case of the Schmandt and Lin (2014) model, the degree of anticorrelation remains above  $-0.4$  to a depth of 125 km (Figure 6). Taking both of these correlation coefficient curves into account, as well as the fact that the high-anticorrelation depths are at the bottom of the Shen and Ritzwoller (2016) model, we focus further discussion in comparing our attenuation model with the Schmandt and Lin (2014) model at 90 km depth. We note that lateral variations in velocity in these models are very similar between 50 and 150 km and the choice of depth does not change our subsequent conclusions.

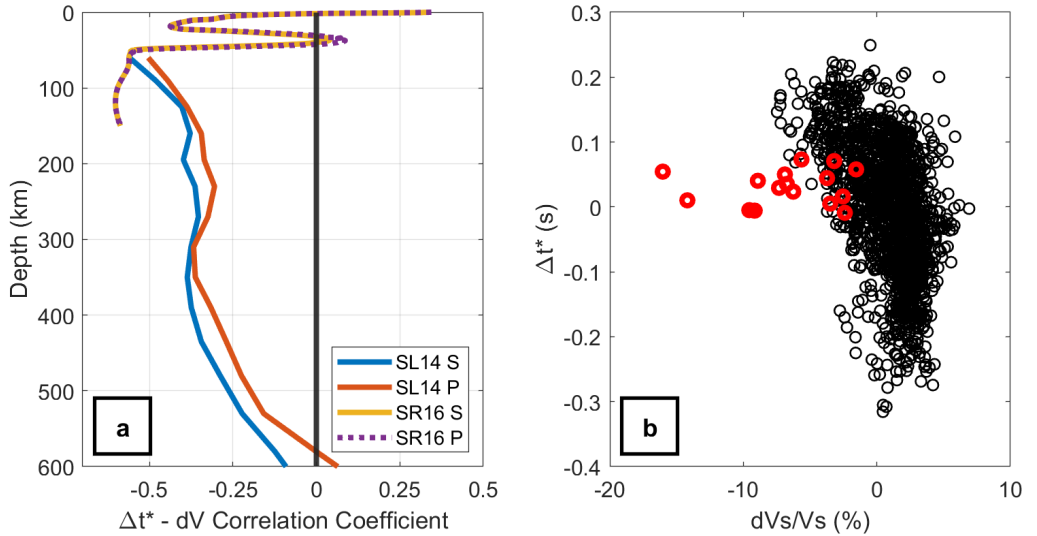


**Figure 6.** Correlation between our  $\Delta t^*$  map and P and S velocity anomaly values as a function of depth. The different curves represent correlation with the Schmandt and Lin (2014) model (SL14 in the legend) and the Shen and Ritzwoller (2016) model (SR16 in the legend). Scatter plot of  $\Delta t^*$  versus  $dV_s/V_s$  at 90 km in the model of Schmandt and Lin (2014). Red open circles correspond to model cells in the eastern Snake River Plain – Yellowstone area.

Although the anticorrelation is strong, the plot of  $\Delta t^*$  versus  $dV_s/V_s$  shows substantial scatter (Figure 6b). Most features of the attenuation model closely mimic those found in velocity models, but in some locations, there is little correspondence between the two sets of seismic observables. In the following subsections, we detail the different relationship between velocity, tectonic history, and the attenuation model for different regions.

#### 4.1.1 The Snake River Plain – Yellowstone

Yellowstone and the eastern Snake River Plain are characterized in seismic velocity models by large-amplitude low-velocity anomalies. At depths of 90 km,  $dV_s/V_s$  anomalies exceed 10% (Schmandt & Lin, 2014). As mentioned in section 3, we do not find the corresponding high attenuation anomaly that one would expect. The TA should provide adequate station coverage to recover this anomaly. For example, the spatial extent of the SRP-Y anomaly is comparable to that of the high-velocity anomaly at the core of the Colorado Plateau (Figure 5), for which we image the expected low-attenuation counterpart anomaly. Additionally, there are several other attenuation anomalies in the map that have a similar or smaller spatial extent. Therefore, the missing SRP-Y anomaly is not the result of insufficient spatial resolution.

Looking at a profile of velocity and attenuation anomalies perpendicular to the trend of the SRP (Figure 7, profile A-A'), we see that the large local minimum in velocity is superimposed on a slight gradient from higher background velocities in the SE to lower (neutral) velocity anomalies in the NW. The broad pattern of attenuation is consistent with this regional trend as it goes from lower attenuation in the SE to higher attenuation in the NW (Figure 7, profile A-A'). Instead of a large increase in attenuation over the SRP, though, we find a small local reduction in attenuation. Removing the regional trends makes this minimum in attenuation clearer (Figure S1).

We consider three possible interpretations. First, the minimum in attenuation is small relative to the standard error of the model (Figure S2), and so while the missing positive anomaly in the SRP-Y cannot be explained by random errors in the data, the superimposed minimum may not be robust. Second, focusing effects could obscure a positive anomaly in attenuation given the strength of the anomaly in velocity. At the length-scales of this study,  $\sim 1$  Hz P waves will not typically feature focusing artifacts (Byrnes et al., 2019) but give the station coverage and the strength of the anomaly focusing effects should be considered further. Note that the attenuation anomaly in the SRP-Y does not appear in models of surface wave attenuation (Bao et al., 2016), and focusing effects are

a likely explanation given the longer periods involved. Third, the minimum in attenuation is consistent with the low attenuation imaged by Adams and Humphreys(2010) in the Yellowstone region. Adams and Humphreys (2010) proposed that the weak attenuation was due to dehydration of the upper mantle due to melting, with melt not enhancing attenuation (Hammond & Humphreys, 2000). Further studies considering our first two interpretations are needed to confirm the minimum in attenuation for P waves in this region.

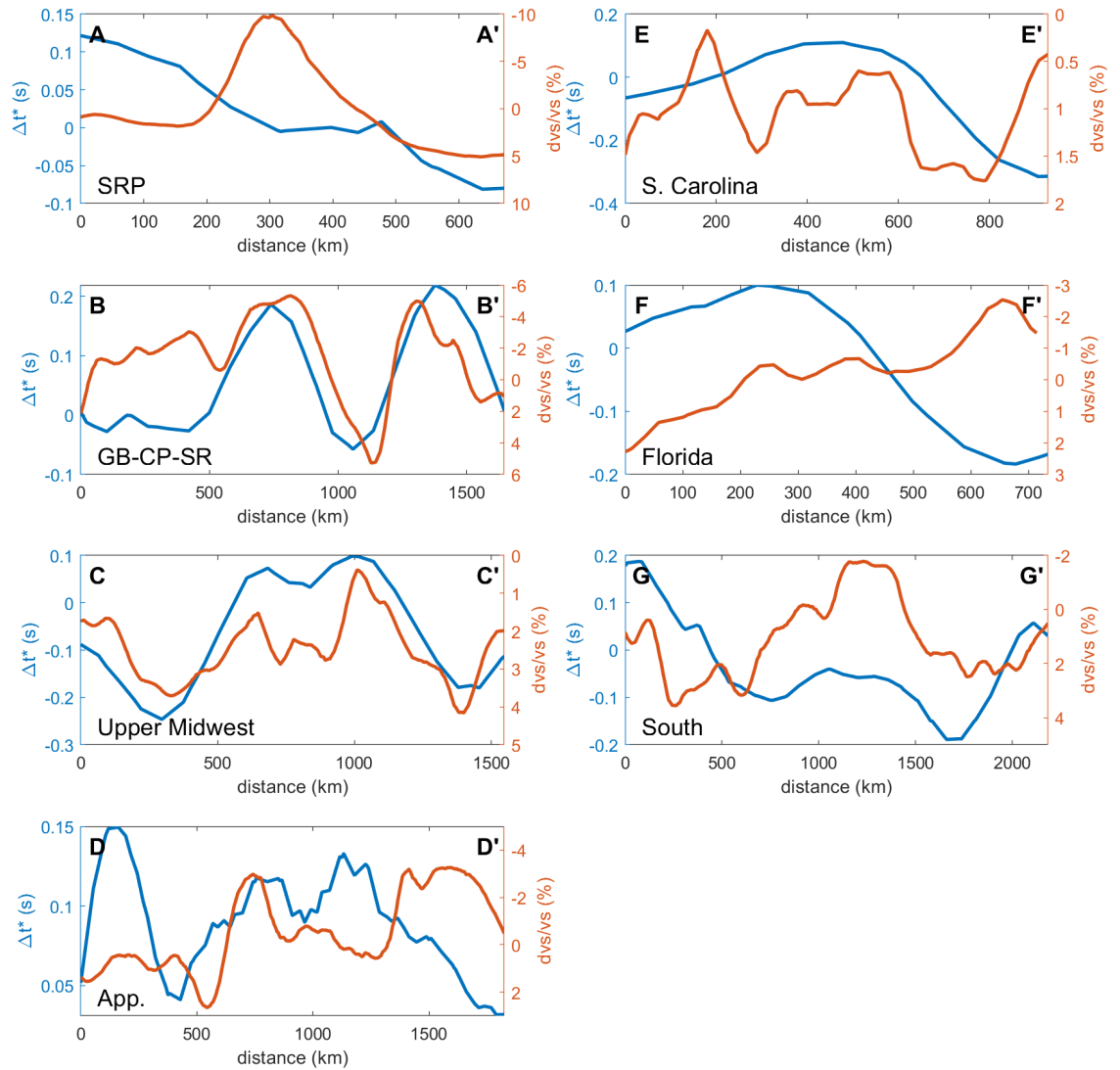


**Figure 7.** Comparison of  $\Delta t^*$  from this study and  $dV_s/V_s$  at 90 km in the model of Schmandt and Lin (2014) along different profiles. For the location of the profiles, see Figure 5. Note that the axis for  $dV_s/V_s$  is inverted (i.e. values increase downward) to facilitate comparison between the two sets of observations. Abbreviations: GB – Great Basin; CP – Colorado Plateau; SR – Southern Rockies; App. – Appalachians.

#### 4.1.2 The Great Basin, Colorado Plateau and Southern Rockies

The core of the CP stands out in seismic velocity models as an isolated patch of relatively high velocities surrounded by low velocities on the west, south and east (e.g. Schmandt & Lin, 2014; Shen & Ritzwoller, 2016). Our model is consistent with these observations, with lower attenuation in the core of the CP than on the flanks. East of the CP, the attenuation results also conform to expectations with high attenuation in the Southern Rockies (SR) and the Rio Grande Rift area, where low velocities have been observed. West of the CP, the Great Basin (GB) typically appears in velocity models as universally slow with minor internal fluctuations. However, although the eastern GB shows higher than average attenuation in our model, the northwestern GB shows negative relative attenuation. This seemingly odd observation becomes more interesting if we compare  $\Delta t^*$  and  $dV_s/V_s$  at 90 km depth along a profile from the northwestern GB to the SR (Figure 7, profile B-B'). We observe that on either side of the Colorado Plateau a change in  $dV_s/V_s$  of 9.5% (from +4.75% at the core of the CP to -4.75% outside) translates to a change in  $\Delta t^*$  of 0.25 s (from 0.2 to -0.05). Further west (at ~600 km in profile B-B', Figure 9), a drop in  $\Delta t^*$  corresponds to an increase in  $dV_s/V_s$ . Although the increase in  $dV_s/V_s$  is modest (~3.7%, only about 40% of the range inside and outside the CP), it corresponds to a substantial change in  $\Delta t^*$  of ~0.2 s (80% of the range inside and outside the CP). In sum, we see that attenuation and  $dV_s/V_s$  are anticorrelated, but the proportionality between a drop in  $V_s$  and the corresponding increase in  $\Delta t^*$  changes along this profile.

#### 4.1.3 The Upper Midwest

Velocity anomalies in the north-central U.S., a geographic region often referred to as “the upper Midwest”, are generally positive (i.e. higher than average) as expected for the cratonic core of the continent. In contrast, our attenuation model shows relatively high attenuation in this area, which is puzzling. If we consider a profile going roughly E-W across this region and compare the values of  $\Delta t^*$  and  $dV_s/V_s$  we find that the relative changes in attenuation and shear wave velocity mimic each other quite closely (Figure 7, profile C-C'). Although velocity anomalies are consistently positive along this profile, reductions in  $dV_s/V_s$  coincide with increases in  $\Delta t^*$ . Interestingly, the proportionality between changes in  $\Delta t^*$  and  $dV_s/V_s$  is substantially larger here than in other parts of the model. The range in  $dV_s/V_s$  along this profile is only ~2.8%, whereas the range in  $\Delta t^*$  exceed 0.3 s. This is larger than the change in  $\Delta t^*$  associated with a nearly 10% change in  $dV_s/V_s$  across the Colorado Plateau as described in the previous subsection.

#### 4.1.4 The Appalachians

The Appalachian Mountains are characterized by high attenuation and low velocity anomalies. There are two distinct low-velocity anomalies that have received attention in the literature recently, the Northern Appalachian Anomaly (Dong & Menke, 2017; Goldhagen et al., 2022; Levin et al., 2018; Menke et al., 2016, 2018) and the Central Appalachian Anomaly (e.g. Byrnes et al., 2019; Evans et al., 2019; Long et al., 2021). The origin of these anomalies is still debated, including whether they have similar or perhaps connected origins, but thinned lithosphere and mantle upwelling is implicated in both cases (e.g. Byrnes et al., 2019; Goldhagen et al., 2022; Long et al., 2021; Menke et al., 2018). Consequently, positive attenuation is expected.

In our model there are three attenuation highs along the Appalachian trend (Figure 7, profile D-D'). The southernmost one is the most prominent reaching  $\Delta t^*$  of 0.15 s. Interestingly, this does not correspond to a conspicuous velocity anomaly in the Schmandt and Lin (2014) model at 90 km depth (Figure 7, profile D-D'). In fact, velocity anomalies in this part of the Appalachians are faster than average. We note, however, that there is a small local reduction in velocity that spatially coincides with the peak in attenuation we observe, and that deeper in the Schmandt and Lin (2014) model there is a spatially small low-velocity anomaly in this area that Carrero Mustellier and Menke (2021) refer to as the Southern Appalachian Anomaly. Shrivastava et al. (2021) image a high-attenuation area in this region that is broadly consistent with our results but their anomaly is not as localized as in our model. The second Appalachian attenuation peak (from south to north) corresponds closely to the CAA, although there is a spatial shift in the peaks of  $\sim 70$  km. This attenuation peak was studied using a denser local data set by Byrnes et al. (2019) (see section 4.2 below). The northernmost anomaly in our model is substantially displaced to the south with respect to the NAA in velocity models (e.g. Schmandt & Lin, 2014). In fact, toward the northern end of the Appalachians attenuation in our model decreases, contrary to what would be expected from the velocity models and to the high attenuation found by Dong and Menke (2017).

#### 4.1.5 Low attenuation regions in the southeastern U.S.

The prominent low attenuation regions in the central Gulf coast, eastern South Carolina and southern Florida, do not correlate with velocity. These features are statistically robust (Figure S2) though lie near the edge of station coverage. Each anomaly occurs in a tile processed independently by two analysts and appear in the same places (Figure 4), though the amplitudes differ at level near the error. The western boundary of the South Carolina anomaly aligns with the edge of the Appalachian piedmont, which suggests consistency with geological boundaries. However, comparing the attenuation and velocity models we do not find any clear correlation. There is a block of relatively high velocities in this area, but velocities sharply decrease toward the coast, whereas attenuation is lowest at the coast (Figure 7, profile E-E'). In Florida, both attenuation and velocity tend to decrease toward the south. Here again, there is little to no

correlation of the smaller features, but the general trends show the opposite of what would be expected: velocity and attenuation trending in the same direction (Figure 7, profile F-F'). Finally, the low attenuation feature in southern Alabama does show some correlation with velocity structure. An EW profile shows a significant increase in velocity ( $dV_s/V_s$  from -2% to ~2%) that spatially coincides with the decrease in attenuation (Figure 7, profile G-G'). We note that Carrero Mustellier and Menke (2021) find a high-velocity anomaly in this general area that they term the Suwannee Block given its spatial association with the Suwannee Terrane of Mueller et al. (2014). However, the Terrane as described by Mueller et al. (2014) lies further east and south, and the center of our attenuation anomaly occurs ~150 km west of the center of the velocity anomaly described by Carrero Mustellier and Menke (2021). A low-attenuation anomaly is also imaged in this region by Shrivastava et al. (2021) although it is spatially smaller than ours than centered ~100 km further north. These discrepancies notwithstanding, it is an intriguing possibility that the imaged anomalies may outline an accreted terrane transferred to Laurentia from Gondwana.

#### 4.2 Relationship to local attenuation studies

The method we employ here for measuring  $\Delta t^*$  has been used in other regional studies in the continental US (Byrnes et al., 2019; Byrnes & Bezada, 2020; Zhu et al., 2021). These studies include data from denser temporary seismic array deployments with station spacing below the nominal 70 km value of the USArray Transportable array. In particular, the Zhu et al. (2021) model for northern Wyoming and surrounding regions uses data from the BASE (e.g. Worthington et al., 2016) and CIELO (Ford et al., 2021) deployments, the latter having average station spacing of 19 km, which locally decreased to 4 km. The study of Byrnes et al. (2019) across the Central Appalachians utilizes data from the MAGIC array (Long et al., 2020) with a station spacing between 30 and 15 km. These denser deployments allow for higher resolution imaging, and the studies in question used a trans-dimensional Bayesian approach to building the  $\Delta t^*$  map that is designed for better recovering sharp gradients (Byrnes et al., 2019). In this section we assess the limits of the resolution of our model by comparing it to the higher-resolution models across two profiles.

In Wyoming, we find that our continental-scale model recovers only the broad trend of decreasing attenuation from west to east, but not the small scale (~100 km width or narrower) features that can be seen superimposed on this trend in the regional model (Figure 8, profile H-H'). Similarly, on the profile across the Central Appalachians, we see that our continental-scale model recovers a substantially smoother version of the regional model. Instead of the sharp gradients on either side of the high-attenuation anomaly, we see a broad and gently sloping peak (Figure 8, profile I-I'). Additionally, the local maximum in attenuation is shifted to the east by ~100 km with respect to the regional model. We conclude that even though our model reveals substantial short-wavelength lateral variations in attenuation structure, it is still a smooth representation of the true structure. As a corollary, continental lithospheric structure likely possesses even

more lateral heterogeneity than what is suggested by our attenuation model. A comparison with the model of Byrnes and Bezada, (2020) for the Salton Trough is not shown since the array used in that study is approximately 100 km long and the model of this study does not vary across the profile.

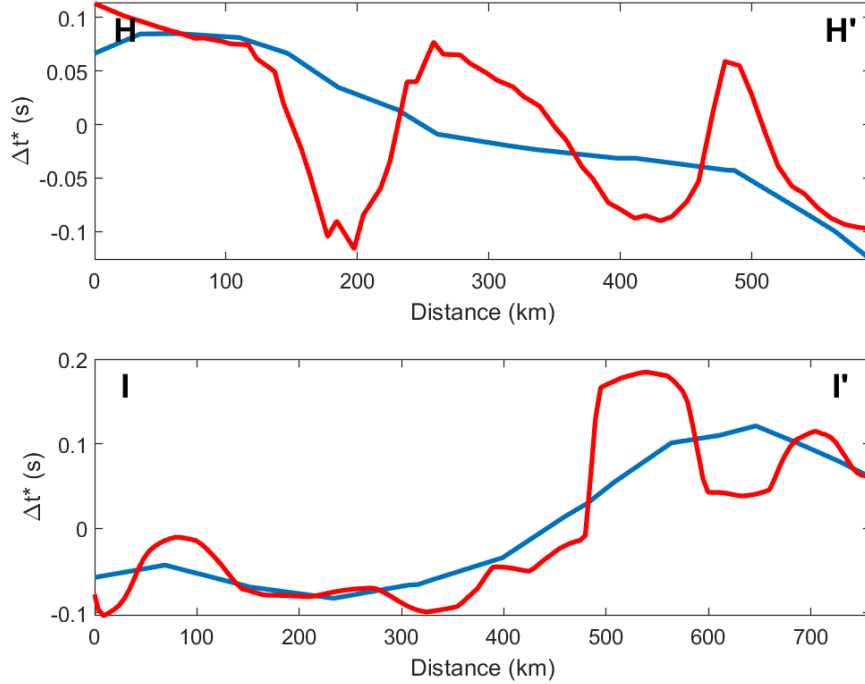


**Figure 8.**  $\Delta t^*$  from this study (blue lines) and from higher resolution studies (red lines) across profiles in Wyoming (H-H', Zhu et al., 2021) and the Central Appalachian Anomaly (I-I', Byrnes et al, 2019). In each case, the mean value across the profile has been removed to facilitate the comparison. For the location of the profiles, see Figure 5.

#### 4.3 Relationship to Seismicity

In this section we explore if a relationship between lateral variations in attenuation and the distribution of intracontinental seismicity exists. A previous study identified a link between rates of intracontinental seismicity and attenuation in Australia (Bezada & Smale, 2019), with seismicity being more abundant where attenuation is high and at some sharp gradients in  $\Delta t^*$ . Using attenuation as a proxy for lithospheric rheology, the latter would be in line with the hypothesis that lateral changes in lithospheric rheology can lead to the localization of stresses and thus to enhanced rates of seismicity (e.g. Mooney et al., 2012).

We observe both in the coterminous US: areas where there is a strong correla-

tion between intracontinental seismicity and large gradients in  $\Delta t^*$  and areas where very large gradients in  $\Delta t^*$  are not associated with any seismicity. The most prominent example of an association between seismicity and attenuation structure is the intermountain seismic belt. South of Yellowstone, seismicity occurs in the transition from the high attenuation regions in the Basin and Range Province to the west and the lower attenuation regions in the core of the Colorado Plateau and SW Wyoming to the east (Figure 9, profiles J-J', K-K', L-L'). North of the Snake River Plain, two belts of seismicity bracket a local attenuation high, although the spatial association is less clear than further south (Figure 9, profile M-M'). Under the assumption that seismic velocity anomalies are a proxy for temperature anomalies, previous studies have made the case that large gradients in dynamic topography may be the underlying cause of the intermountain seismic belt (Becker et al., 2015). We suggest that an alternative explanation is that the gradients in seismic velocity and attenuation represent rheological boundaries that lead to a localization of stresses.

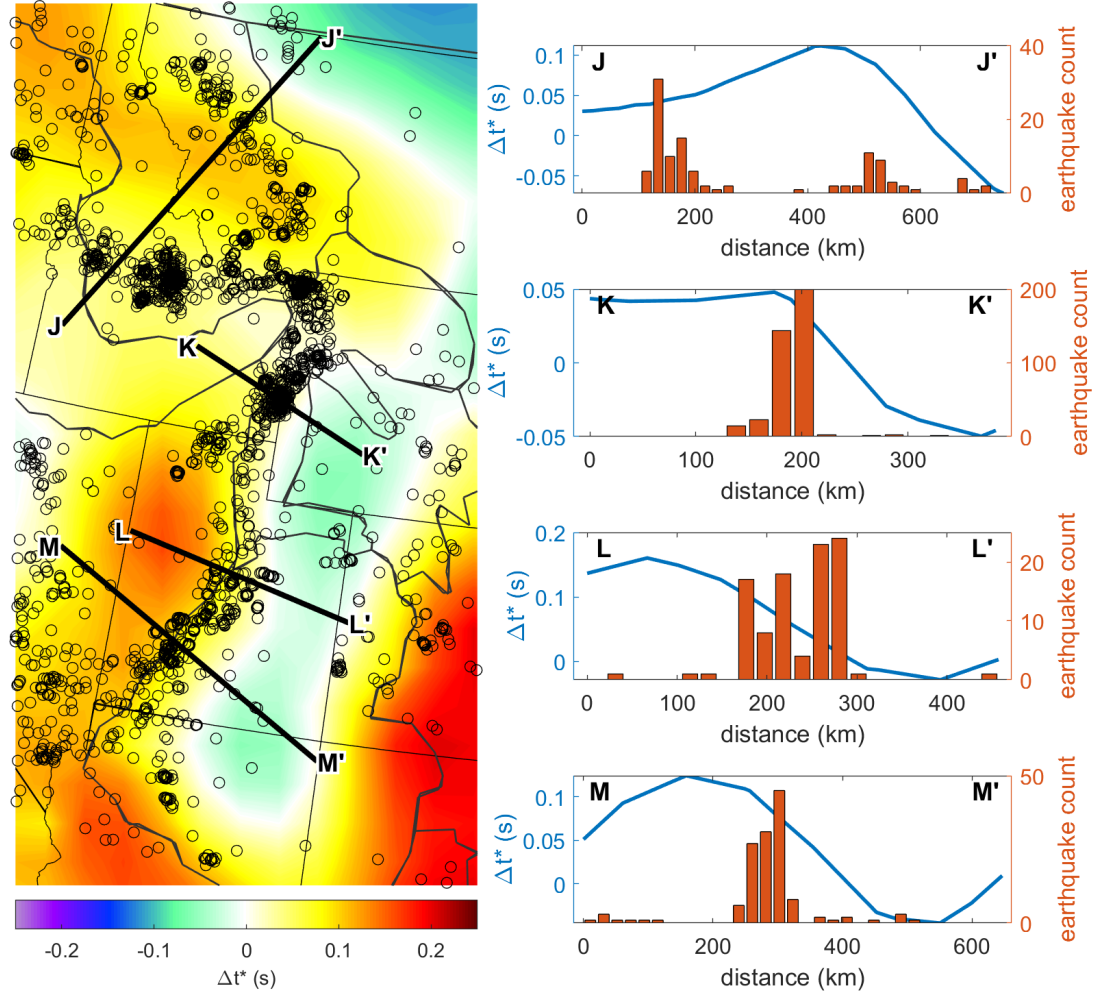


**Figure 9.** Map of  $\Delta t^*$  in the Intermountain Seismic Belt region with earthquakes from the USGS catalog (left) and plots showing  $\Delta t^*$  and histograms of earthquake count along different profiles (right). Earthquakes are counted if they occur within 50 km of the profile.

Notable counter-examples include the boundaries of the low attenuation band in the Great Plains, the low-attenuation block east of the southern Appalachian Piedmont and low attenuation blocks in southern Florida and the central Gulf Coast; no significant seismicity is associated with these blocks (Figure S3). Unlike in Australia (Bezada and Smale, 2019), we do not see concentrations of seismicity that coincide with the highest-attenuation regions in the model, yet there is a band of seismicity that follows the high-attenuation region in the

Appalachians (Figure S3).

Another interesting region is the Reelfoot Rift (Figure 10). There, we see that the seismicity correlates with low attenuation, contrary to expectations. Toward the north of the seismically active region, earthquakes cluster near the local minimum of attenuation (Figure 10, profile N-N'), whereas toward the south, seismicity peaks to the west of the minimum, in what could be called the end of the transition between high and low attenuation (Figure 10, profile O-O'). We speculate that there may be a small low-attenuation block that is broadened by a combination of the inversion regularization and the density of the stations (see section 4.2). Taken at face value, however, this result suggests the Reelfoot Rift seismicity occurs near the core of a relatively low attenuation block (and presumably relatively strong lithosphere).

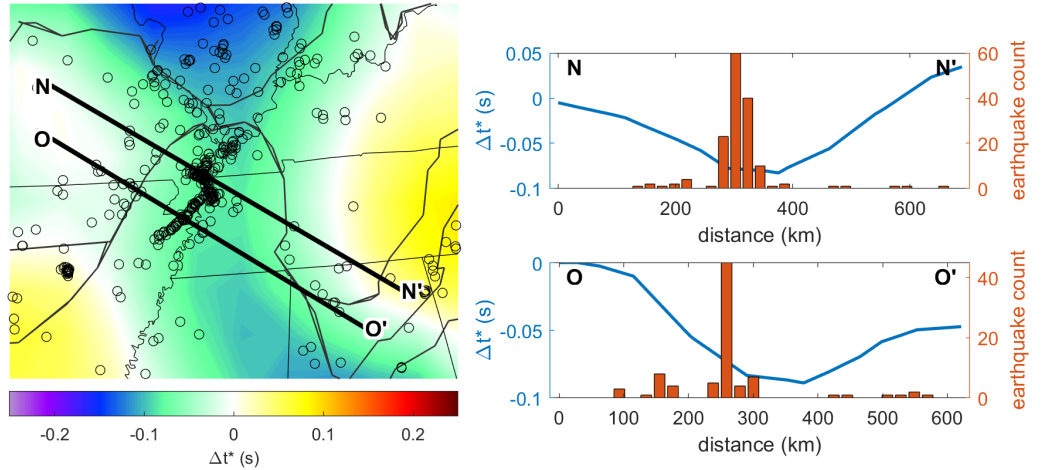


**Figure 10.** Map of  $\Delta t^*$  in the Reelfoot Rift region with earthquakes from the USGS catalog (left) and plots showing  $\Delta t^*$  and histograms of earthquake count along different profiles (right). Earthquakes are counted if they occur within 50 km of the profile.

We note that a contrast in rheology would not be sufficient to cause increased seismicity, but regional stresses need to be high enough. Future work should explore how lateral changes in lithospheric rheology that follow the attenuation structure we image interact with regional stresses to see where high seismicity rates would be predicted.

## 5 Conclusions

We measure P-wave teleseismic attenuation across the conterminous United States by analyzing data from deep earthquakes recorded by EarthScope Transportable Array stations. We divide the large study area into 12 tiles that are analyzed independently. Repeat analysis of four of the tiles shows consistent results, indicating that subjective choices made by analysts do not substan-

tially impact the features in the final model. The set of all the attenuation measurements are inverted together to create a smooth map of the differential attenuation across the study area. As expected, attenuation is generally higher in the western than in the eastern United States and attenuation and seismic velocity at 90 km depth are anti-correlated. However, significant short wavelength variations sometimes break this expectation. A given change in velocity can correspond to either relatively large or relatively small changes in attenuation depending on the region. One notable example is the contrast between the Great Basin and the Colorado Plateau. In the Great Basin, a modest velocity anomaly in the west corresponds to a large change in attenuation, whereas in the region of the Colorado Plateau a much larger change in velocity corresponds to approximately the same changes in attenuation across the Great Basin (Figure 7, profile B-B'). Attenuation along the Appalachian Mountains is relatively high and punctuated by three distinct anomalies that partially correspond to distinct seismic velocity anomalies identified in previous studies (Figure 7, profile D-D'). In the Upper Midwest, we find that attenuation near the cratonic core is relatively high. While surprising, this trend correlates well with local reductions in seismic velocity (Figure 7, profile C-C'). One of our most intriguing results is the absence of a high-attenuation anomaly in the Snake River Plain despite the very low seismic velocities imaged there. Deciphering the physical mechanisms that can lead to the observed combinations of seismic velocity and seismic attenuation is beyond the scope of the study and we propose it as a fertile topic for future research. We also find that intracontinental seismicity shows some correlation with gradients in attenuation in the Intermountain Seismic Belt and the Reelfoot Rift (Figure 9, 10), but other and sometimes larger gradients in attenuation are not associated with increased seismicity. Finally, we note that although our study reveals substantial lateral heterogeneity in attenuation, a comparison with higher-resolution studies using denser station deployments strongly suggests that true attenuation structure has even smaller spatial length scale variations (Figure 8).

### **Acknowledgments**

To be completed after review.

### **Open Research**

All the data used in this study is available through the IRIS Data Management Center. The relevant networks are USArray Transportable Array (network code TA, <https://doi.org/10.7914/SN/TA>) and the Southern California Seismic Network (network code CI, <https://doi.org/10.7914/SN/CI>). The waveforms used for analysis will be archived in a UMN digital repository. Details on this, and the relevant link, will be added after acceptance of the manuscript.

### **References**

Adams, D. C., & Humphreys, E. D. (2010). New constraints on the properties

of the Yellowstone mantle plume from P and S wave attenuation tomography. *Journal of Geophysical Research: Solid Earth*, 115(B12), n/a-n/a. <https://doi.org/10.1029/2009JB006864>

Azimi, S. A., Kalinin, A. V., Kalinin, V. V., & Pivovarov, B. L. (1968). Impulse and transient characteristics of media with linear and quadratic absorption laws. *Izv. Phys. Solid Earth*, 2, 88–93.

Bao, X., Dalton, C. A., Jin, G., Gaherty, J. B., & Shen, Y. (2016). Imaging Rayleigh wave attenuation with USArray. *Geophysical Journal International*, 206(1), 241–259. <https://doi.org/10.1093/gji/ggw151>

Becker, T. W. (2012). On recent seismic tomography for the western United States. *Geochemistry, Geophysics, Geosystems*, 13(1), Q01W10. <https://doi.org/10.1029/2011GC003977>

Becker, Thorsten W., Lowry, A. R., Faccenna, C., Schmandt, B., Borsa, A., & Yu, C. (2015). Western US intermountain seismicity caused by changes in upper mantle flow. *Nature*, 524(7566), 458–461. <https://doi.org/10.1038/nature14867>

Bezada, M. J., & Smale, J. (2019). Lateral Variations in Lithospheric Mantle Structure Control the Location of Intracontinental Seismicity in Australia. *Geophysical Research Letters*, 46(22), 12862–12869. <https://doi.org/10.1029/2019GL084848>

Bezada, M. J., Byrnes, J., & Eilon, Z. (2019). On the robustness of attenuation measurements on teleseismic P waves: insights from micro-array analysis of the 2017 North Korean nuclear test. *Geophysical Journal International*, 218(1), 573–585. <https://doi.org/10.1093/gji/ggz169>

Bezada, Maximiliano J. (2017). Insights into the lithospheric architecture of Iberia and Morocco from teleseismic body-wave attenuation. *Earth and Planetary Science Letters*, 478, 14–26. <https://doi.org/10.1016/j.epsl.2017.08.029>

Bodmer, M., Toomey, D. R., Hooft, E. E. E., & Schmandt, B. (2018). Buoyant Asthenosphere Beneath Cascadia Influences Megathrust Segmentation. *Geophysical Research Letters*, 45(14), 6954–6962. <https://doi.org/10.1029/2018GL078700>

Buehler, J. S., & Shearer, P. M. (2017). Uppermost mantle seismic velocity structure beneath USArray. *Journal of Geophysical Research: Solid Earth*, 122(1), 436–448. <https://doi.org/10.1002/2016JB013265>

Byrnes, J. S., & Bezada, M. (2020). Dynamic Upwelling Beneath the Salton Trough Imaged With Teleseismic Attenuation Tomography. *Journal of Geophysical Research: Solid Earth*, 125(11), e2020JB020347. <https://doi.org/10.1029/2020JB020347>

Byrnes, J. S., Bezada, M., Long, M. D., & Benoit, M. H. (2019). Thin lithosphere beneath the central Appalachian Mountains: Constraints from seismic

- attenuation beneath the MAGIC array. *Earth and Planetary Science Letters*, 519, 297–307. <https://doi.org/10.1016/j.epsl.2019.04.045>
- Cafferky, S., & Schmandt, B. (2015). Teleseismic P wave spectra from USArray and implications for upper mantle attenuation and scattering. *Geochemistry, Geophysics, Geosystems*, 16(10), 3343–3361. <https://doi.org/10.1002/2015GC005993>
- Carrero Mustelier, E., & Menke, W. (2021). Seismic anomalies in the southeastern North American asthenosphere as characterized with body wave travel times from high-quality teleseisms. *Tectonophysics*, 809, 228853. <https://doi.org/10.1016/j.tecto.2021.228853>
- Chantel, J., Manthilake, G., Andrault, D., Novella, D., Yu, T., & Wang, Y. (2016). Experimental evidence supports mantle partial melting in the asthenosphere. *Science Advances*, 2(5), e1600246. <https://doi.org/10.1126/sciadv.1600246>
- Cline Ii, C. J., Faul, U. H., David, E. C., Berry, A. J., & Jackson, I. (2018). Redox-influenced seismic properties of upper-mantle olivine. *Nature*, 555(7696), 355–358. <https://doi.org/10.1038/nature25764>
- Deng, Y., Byrnes, J. S., & Bezada, M. (2021). New Insights Into the Heterogeneity of the Lithosphere-Asthenosphere System Beneath South China From Teleseismic Body-Wave Attenuation. *Geophysical Research Letters*, 48(6), e2020GL091654. <https://doi.org/10.1029/2020GL091654>
- Dong, M. T., & Menke, W. H. (2017). Seismic High Attenuation Region Observed Beneath Southern New England From Teleseismic Body Wave Spectra: Evidence for High Asthenospheric Temperature Without Melt. *Geophysical Research Letters*, 44(21), 10,958-10,969. <https://doi.org/10.1002/2017GL074953>
- Eilon, Z. C., & Abers, G. A. (2017). High seismic attenuation at a mid-ocean ridge reveals the distribution of deep melt. *Science Advances*, 3(5), e1602829. <https://doi.org/10.1126/sciadv.1602829>
- Evans, Rob. L., Benoit, M. H., Long, M. D., Elsenbeck, J., Ford, H. A., Zhu, J., & Garcia, X. (2019). Thin lithosphere beneath the central Appalachian Mountains: A combined seismic and magnetotelluric study. *Earth and Planetary Science Letters*, 519, 308–316. <https://doi.org/10.1016/j.epsl.2019.04.046>
- Faul, U. H., & Jackson, I. (2005). The seismological signature of temperature and grain size variations in the upper mantle. *Earth and Planetary Science Letters*, 234(1), 119–134. <https://doi.org/10.1016/j.epsl.2005.02.008>
- Faul, U. H., Fitz Gerald, J. D., & Jackson, I. (2004). Shear wave attenuation and dispersion in melt-bearing olivine polycrystals: 2. Microstructural interpretation and seismological implications. *Journal of Geophysical Research: Solid Earth*, 109(B6). <https://doi.org/10.1029/2003JB002407>
- Ford, H. A., Bezada, M. J., Byrnes, J. S., Birkey, A., & Zhu, Z. (2021). The

- CIELO Seismic Experiment. *Seismological Research Letters*. <https://doi.org/10.1785/0220210237>
- Goldhagen, G. B., Ford, H. A., & Long, M. D. (2022). Evidence for a lithospheric step and pervasive lithospheric thinning beneath southern New England, northeastern USA. *Geology*, 50(9), 1078–1082. <https://doi.org/10.1130/G50133.1>
- Hammond, W. C., & Humphreys, E. D. (2000). Upper mantle seismic wave velocity: Effects of realistic partial melt geometries. *Journal of Geophysical Research-Solid Earth*, 105(B5), 10975–10986. <https://doi.org/10.1029/2000JB900041>
- Hawley, W. B., Allen, R. M., & Richards, M. A. (2016). Tomography reveals buoyant asthenosphere accumulating beneath the Juan de Fuca plate. *Science*, 353(6306), 1406–1408. <https://doi.org/10.1126/science.aad8104>
- Hopper, E., & Fischer, K. M. (2018). The Changing Face of the Lithosphere-Asthenosphere Boundary: Imaging Continental Scale Patterns in Upper Mantle Structure Across the Contiguous U.S. With Sp Converted Waves. *Geochemistry, Geophysics, Geosystems*, 19(8), 2593–2614. <https://doi.org/10.1029/2018GC007476>
- Jackson, I., & Faul, U. H. (2010). Grainsize-sensitive viscoelastic relaxation in olivine: Towards a robust laboratory-based model for seismological application. *Physics of the Earth and Planetary Interiors*, 183(1–2), 151–163. <https://doi.org/10.1016/j.pepi.2010.09.005>
- Lawrence, J. F., Shearer, P. M., & Masters, G. (2006). Mapping attenuation beneath North America using waveform cross-correlation and cluster analysis. *Geophys. Res. Lett.*, 33, L07315.
- Levin, V., Long, M. D., Skryzalin, P., Li, Y., & López, I. (2018). Seismic evidence for a recently formed mantle upwelling beneath New England. *Geology*, 46(1), 87–90. <https://doi.org/10.1130/G39641.1>
- Lin, F.-C., & Schmandt, B. (2014). Upper crustal azimuthal anisotropy across the contiguous U.S. determined by Rayleigh wave ellipticity. *Geophysical Research Letters*, 41(23), 8301–8307. <https://doi.org/10.1002/2014GL062362>
- Liu, H., Byrnes, J. S., Bezada, M., Wu, Q., Pei, S., & He, J. (2022). Variable Depths of Magma Genesis in the North China Craton and Central Asian Orogenic Belt Inferred From Teleseismic P Wave Attenuation. *Journal of Geophysical Research: Solid Earth*, 127(3), e2021JB022439. <https://doi.org/10.1029/2021JB022439>
- Long, M. D., Benoit, M. H., Evans, R. L., Aragon, J. C., & Elsenbeck, J. (2020). The MAGIC Experiment: A Combined Seismic and Magnetotelluric Deployment to Investigate the Structure, Dynamics, and Evolution of the Central Appalachians. *Seismological Research Letters*, 91(5), 2960–2975. <https://doi.org/10.1785/0220200150>

- Long, M. D., Wagner, L. S., King, S. D., Evans, R. L., Mazza, S. E., Byrnes, J. S., et al. (2021). Evaluating Models for Lithospheric Loss and Intraplate Volcanism Beneath the Central Appalachian Mountains. *Journal of Geophysical Research: Solid Earth*, 126(10), e2021JB022571. <https://doi.org/10.1029/2021JB022571>
- Malinverno, A., & Briggs, V. A. (2004). Expanded uncertainty quantification in inverse problems: Hierarchical Bayes and empirical Bayes. *GEOPHYSICS*, 69(4), 1005–1016. <https://doi.org/10.1190/1.1778243>
- Menke, W., Skryzalin, P., Levin, V., Harper, T., Darbyshire, F., & Dong, T. (2016). The Northern Appalachian Anomaly: A modern asthenospheric upwelling. *Geophysical Research Letters*, 43(19), 10,173–10,179. <https://doi.org/10.1002/2016GL070918>
- Menke, W., Lamoureaux, J., Abbott, D., Hopper, E., Hutson, D., & Marrero, A. (2018). Crustal Heating and Lithospheric Alteration and Erosion Associated With Asthenospheric Upwelling Beneath Southern New England (USA). *Journal of Geophysical Research: Solid Earth*, 123(10), 8995–9008. <https://doi.org/10.1029/2018JB015921>
- Mooney, W. D., Ritsema, J., & Hwang, Y. K. (2012). Crustal seismicity and the earthquake catalog maximum moment magnitude ( $M_{\text{cmax}}$ ) in stable continental regions (SCRs): Correlation with the seismic velocity of the lithosphere. *Earth and Planetary Science Letters*, 357–358, 78–83. <https://doi.org/10.1016/j.epsl.2012.08.032>
- Mueller, P. A., Heatherington, A. L., Foster, D. A., Thomas, W. A., & Wooden, J. L. (2014). The Suwannee suture: Significance for Gondwana-Laurentia terrane transfer and formation of Pangaea. *Gondwana Research*, 26(1), 365–373. <https://doi.org/10.1016/j.jgr.2013.06.018>
- Pavlis, G. L., Sigloch, K., Burdick, S., Fouch, M. J., & Vernon, F. L. (2012). Unraveling the geometry of the Farallon plate: Synthesis of three-dimensional imaging results from USArray. *Tectonophysics*, 532–535, 82–102. <https://doi.org/10.1016/j.tecto.2012.02.008>
- Porritt, R. W., Becker, T. W., Boschi, L., & Auer, L. (2021). Multiscale, radially anisotropic shear wave imaging of the mantle underneath the contiguous United States through joint inversion of USArray and global data sets. *Geophysical Journal International*, 226(3), 1730–1746. <https://doi.org/10.1093/gji/ggab185>
- Porter, R., Liu, Y., & Holt, W. E. (2016). Lithospheric records of orogeny within the continental U.S. *Geophysical Research Letters*, 43(1), 144–153. <https://doi.org/10.1002/2015GL066950>
- Schmandt, B., & Lin, F.-C. (2014). P and S wave tomography of the mantle beneath the United States. *Geophysical Research Letters*, 41(18), 2014GL061231. <https://doi.org/10.1002/2014GL061231>
- Shen, W., & Ritzwoller, M. H. (2016). Crustal and uppermost mantle structure beneath the United States. *Journal of Geophysical Research: Solid Earth*,

121(6), 2016JB012887. <https://doi.org/10.1002/2016JB012887>

Shrivastava, A., Liu, K. H., & Gao, S. S. (2021). Teleseismic P-Wave Attenuation Beneath the Southeastern United States. *Geochemistry, Geophysics, Geosystems*, 22(6), e2021GC009715. <https://doi.org/10.1029/2021GC009715>

Stanciu, A. C., & Humphreys, E. D. (2020). Upper mantle tomography beneath the Pacific Northwest interior. *Earth and Planetary Science Letters*, 539, 116214. <https://doi.org/10.1016/j.epsl.2020.116214>

Teng, T.-L. (1968). Attenuation of body waves and the Q structure of the mantle. *Journal of Geophysical Research*, 73(6), 2195–2208. <https://doi.org/10.1029/JB073i006p02195>

Whitmeyer, S. J., & Karlstrom, K. E. (2007). Tectonic model for the Proterozoic growth of North America. *Geosphere*, 3(4), 220–259. <https://doi.org/10.1130/GES00055.1>

Worthington, L. L., Miller, K. C., Erslev, E. A., Anderson, M. L., Chamberlain, K. R., Sheehan, A. F., et al. (2016). Crustal structure of the Bighorn Mountains region: Precambrian influence on Laramide shortening and uplift in north-central Wyoming. *Tectonics*, 35(1), 2015TC003840. <https://doi.org/10.1002/2015TC003840>

Yamauchi, H., & Takei, Y. (2016). Polycrystal anelasticity at near-solidus temperatures. *Journal of Geophysical Research: Solid Earth*, 121(11), 7790–7820. <https://doi.org/10.1002/2016JB013316>

Zhou, T., Li, J., Xi, Z., Li, G., & Chen, M. (2022). CUSRA2021: A Radially Anisotropic Model of the Contiguous US and Surrounding Regions by Full-Waveform Inversion. *Journal of Geophysical Research: Solid Earth*, 127(8), e2021JB023893. <https://doi.org/10.1029/2021JB023893>

Zhu, Z., Bezada, M. J., Byrnes, J. S., & Ford, H. A. (2021). Evidence for Stress Localization Caused by Lithospheric Heterogeneity From Seismic Attenuation. *Geochemistry, Geophysics, Geosystems*, 22(11), e2021GC009987. <https://doi.org/10.1029/2021GC009987>